GT2020-14696

EFFECT OF AXIAL CASING GROOVE GEOMETRY ON ROTOR-GROOVE INTERACTIONS IN THE TIP REGION OF A COMPRESSOR

Subhra Shankha Koley
Johns Hopkins University
Department of Mechanical
Engineering
Baltimore, MD, USA

Huang Chen
Johns Hopkins University
Department of Mechanical
Engineering
Baltimore, MD, USA

Ayush Saraswat
Johns Hopkins University
Department of Mechanical
Engineering
Baltimore, MD, USA

Joseph Katz
Johns Hopkins University
Department of Mechanical
Engineering
Baltimore, MD, USA

ABSTRACT

The present experimental study expands an ongoing effort to characterize the interactions of axial casing grooves (ACGs) with the flow in the tip region of an axial turbomachine. In recent work, we have tested a series of grooves with the same inlet geometry that overlaps with the rotor blade leading edge, but with different exit directions. Two geometries have stood out: The U grooves, which have an outflow in the negative circumferential direction (opposing the blade motion) are the most effective in suppressing stall, achieving as much as 60% reduction in stall flowrate, but cause a 2% decrease in efficiency around the best efficiency point (BEP). In contrast, the S grooves, which have an outflow in the positive circumferential direction, achieve a milder improvement in stall suppression (36%) but do not degrade the performance near BEP. This paper focuses on explaining these trends by measuring the flow in the tip region and within the U and S grooves. The stereo-PIV (SPIV) measurements are performed in the JHU refractive index matched facility, which allows unobstructed observations in the entire machine. Data has been acquired in two meridional planes that intersect with the grooves at different locations, and two radial planes (z, θ), the first coinciding with the blade tip, and the second, with the tip gap. For each plane, data has been acquired at fourteen rotor orientations relative to the grooves to examine the rotor-grooves interactions. At low flow rates, the inflow into both grooves peaks periodically when the blade pressure side (PS) faces the entrance (downstream side) to the grooves. This inflow rolls up into a large vortex that remains and lingers within the groove long after the blade clears the groove. The outflow depends on the shape of the groove. For the S groove, the outflow exits at the upstream end of the groove in the positive circumferential direction, as designed. In contrast, for the U grooves, the fast radially and circumferentially negative outflow peaks at the base of the U. The resulting jet causes substantial periodic variations in the flow angle near the leading edge of the rotor blade. Close to the BEP, the chordwise location of primary blade loading moves downstream, as expected. The inflow into the grooves occurs for a small fraction of the blade passing period, and most of the tip leakage vortex remains in the main flow passage. For the S grooves, the rotor-groove interactions seem to be minimal, with little (but not zero) inflow or outflow at both ends, and minimal changes to the flow angle in the passage. In contrast, for the U groove, the inflow into and outflow from the groove reverse direction (compared to the low flowrate trends), entering at the base of the U, and exiting mostly at its downstream end, especially when the blade is not near. The resulting entrainment of secondary flows from the groove into the passage are likely contributors to the reduced efficiency at BEP for the U grooves.

INTRODUCTION

Mitigating surge and rotating stall in axial turbomachines has been the focus of many studies over the years. It is widely believed that these adverse phenomena are primarily associated with tip leakage flows [1-3], hence endwall casing grooves have shown promise in extending the stall margin [4-6]. This approach usually involves efficiency loss near BEP, with axial casing grooves (ACGs) achieving better stall margin improvement, but higher efficiency loss, compared to circumferential slots [7-12]. There are varying opinions on the extent and mechanisms affecting the efficiency loss [13,14,15,16,17,18], but the gain in
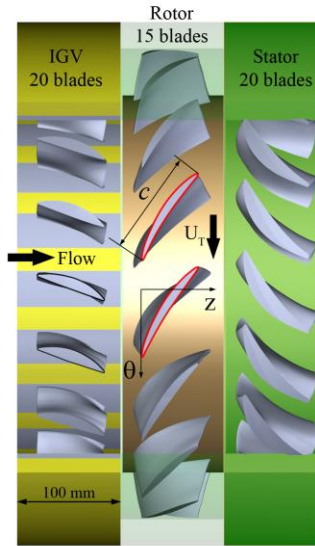
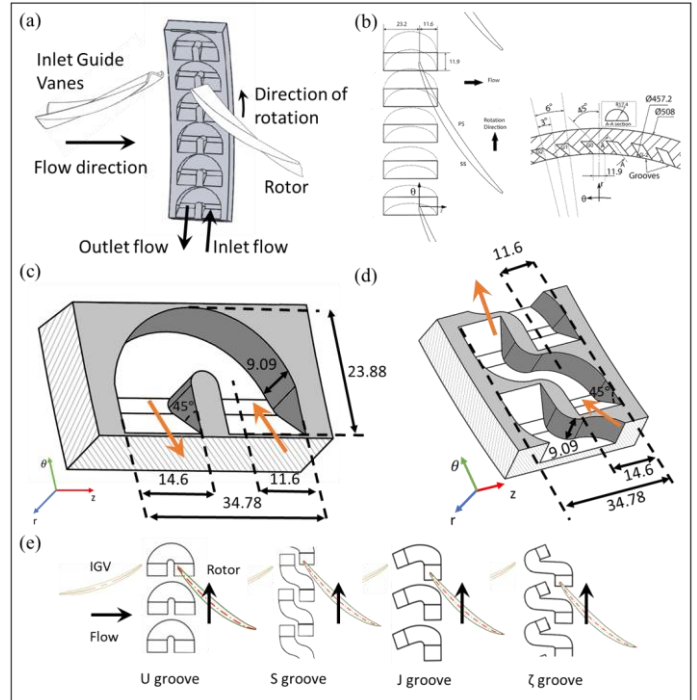Figure 1: Configuration of one and a half stage compressor.

Figure 2: The geometry of the casing grooves: (a) The location of the U grooves with respect to the rotor and IGV blades, (b) The location and orientation of the original semicircular ACGs [13,17,18], (c, d) 3D illustrations of: (c) the U groove, and (d) the S groove, and (e) the shapes, location and orientation of the U, S, J and ζ grooves. All the dimensions are in mm.

stall margin has been attributed to momentum exchange between groove inflow and outflow [10]. Undoubtedly, introduction of grooves makes the tip leakage flow much more complex. Hence, it is important to study the effect of groove-passage flow interactions and determine mechanisms affecting the performance and the efficiency of the turbomachine.

In our previous studies using semi-circular axial casing grooves, introduced initially in [13,17,18], we have also been successful in delaying stall significantly along with the expected loss in BEP efficiency in the one and a half stage turbomachine depicted in Fig. 1. The relevant parameters are provided in Table 1 and the semi-circular grooves are sketched in Fig. 2b. Stereo-PIV measurements in this refractive index-matched facility have shown [17,18] that near stall conditions of the smooth endwall case: (i) parts of tip leakage vortex (TLV) is entrained into the groove, reducing the strength of the remaining part, (ii) the development of secondary structures, such as backflow vortices, which propagate from one passage to the next for the smooth enwall [19], is prevented [17], and (iii) the outflow from the grooves injected in the negative circumferential direction causes periodic changes to the flow angle around the rotor leading edge. In contrast, at high flow rates [17], secondary flow structures developing within the grooves, such as a corner vortex, are entrained by the TLV into the passage, causing TLV fragmentation and increases in tip region turbulence and area occupied by vortex fragments. The grooves also shift the blade loading towards the leading edge.

Aimed at understanding which of the above-mentioned contributors to stall suppression play a primary role, our ongoing effort decouples the effect of periodic modulation of the incident angles from the TLV ingestion. As depicted in Fig. 2 (dimensional details follows), it involves a series of open grooves with the same inlet geometry at the downstream end, but with different outlet directions at the upstream end. The expected outcome has been a similar ingestion in the pressure side of the blade, but different outflow directions at the upstream end. The "U" groove is supposed to direct the outflow in the negative circumferential directions (presumably similar to the semi-circular ACGs), the outlet from the "S" groove is aligned in the positive circumferential direction, and the exit from "ζ" and "J" grooves are aligned with and against the outflow direction from the inlet guide vanes (IGV), respectively. Pressure rise and efficiency tests (presented first in [20]) are shown in Fig. 3a and 3b, respectively. The static-to-static pressure-rise coefficient is $\psi_{SS}=(P_{exit}-P_{in})/0.5\rho U_T^2$, where $P_{exit}-P_{in}$ is the pressure difference across the entire machine. The efficiency is $\eta=(P_{exit}-P_{in})Q/T\Omega$, where Q is the volumetric flow rate, and T is the torque measured by a shaft torque-meter [18] after subtracting the effects of bearings (torque measured when the blades are removed). They show that the U grooves achieve the highest reduction in stall-onset flowrate of about 60%, but cause a 2.0% efficiency loss at BEP compared to the smooth endwall. The S grooves still achieve a substantial stall margin improvement of 36%, but not to the same extent as the U grooves. However, they do not cause reduction in BEP efficiency. Since the changes associated with the ζ and J grooves fall between those of the S and U grooves, subsequent investigations have focused on the groove-passage flow interaction associated with S and U grooves.

Since the initial measurements have been performed using non-transparent groove-containing rings manufactured using rapid-prototyping, the preliminary results presented in [20] consist only of SPIV data obtained in an axial plane located near
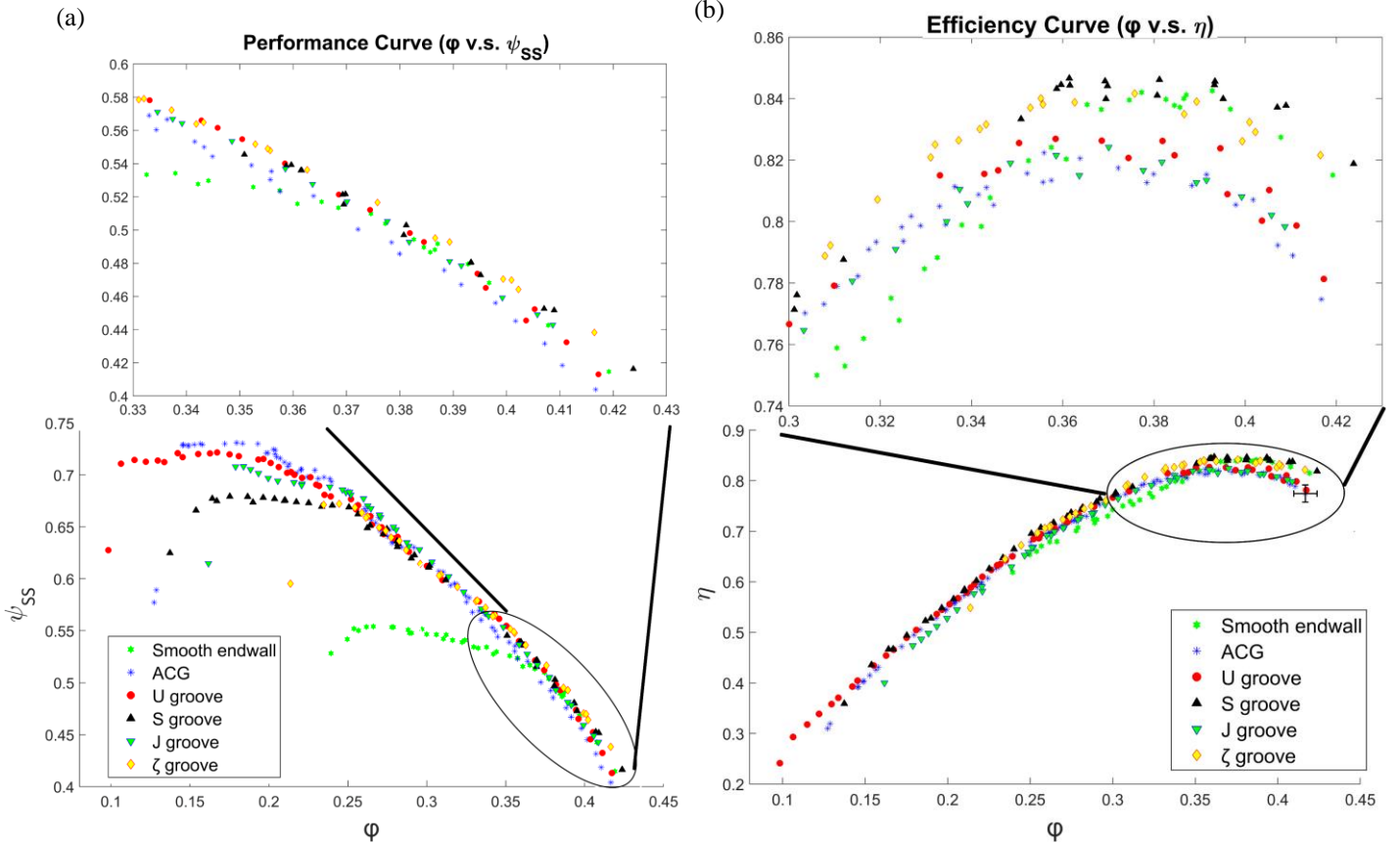
Figure 3: (a) The static to static pressure coefficient for all the grooves, and (b) The corresponding efficiency. The encircled region is shown magnified for clarity. Definitions for ψ and φ are provided in the nomenclature.

the blade trailing edge, far downstream of the grooves. As will be discussed later, they show, while there are small differences between the axial velocity distribution downstream of the U and S grooves, the circumferential velocity distributions are considerably different. At low flowrate the circumferential velocity is higher downstream of the S groove, and at high flow rate, it is higher for the U groove. Apparently, an increase in circumferential velocity correlates with reduced performance. A similar trend has been observed by Houghton and Day [21] for circumferential grooves.

Subsequently, we have manufactured transparent U and S grooves, enabling us to perform detailed flow measurements within and around the grooves and use the data to characterize the effect of outflow direction from the groove on: (i) the passage flow-groove interactions, (ii) evolution and ingestion of the TLV, (iii) pulsatility of the flow angle near the blade leading edge and its impact on performance, (iv) mechanisms affecting the abovementioned differences in circumferential velocity near the blade trailing edge, and (v) causes for difference in efficiency near BEP and stall margin improvements. As described in this paper, to achieve these goals, we have acquired SPIV data in several radial and meridional planes covering both the tip region and the interior of the grooves at flowrates corresponding to pre-stall ($\varphi=0.25$) and BEP ($\varphi=0.38$) conditions for the untreated

endwall. Details of the experimental setup and procedures are provided in the next section. Velocity and vorticity distributions comparing the flow structure in several planes are presented subsequently, followed by a discussion about the implication of our finding. Among the numerous observations, the results show that at low flow rate, while the S groove has the expected outflow direction, the U groove does not. Furthermore, while the S groove has minimal interactions with the passage at BEP, flow injected from the U groove in unexpected locations and direction keeps on disrupting the passage flow.

FACILITY AND GROOVE GEOMETRIES

The one and a half stage axial compressor illustrated in Fig. 1 and the JHU refractive index matched facility have been described in a series of previous studies [17,18,19,20,24,27,28]. The three blade rows consist of a 20 blade inlet guide vanes (IGV), a 15 blade rotor and a 20 blade stator. Relevant geometric and flow parameters are listed in Table 1, and the definition of variables is provided in the nomenclature. The blade profiles are similar to those of the first three rows of the Low-Speed Axial Compressor (LSAC) at NASA Glenn [29], but the aspect ratio has been reduced to facilitate use of acrylic blade in liquid. The working fluid is a concentrated aqueous solution of sodium iodide (NaI) whose refractive index (1.4876) is matched with

3   Copyright © 2020 by ASME

that of the acrylic rotor blades, casing and casing groove rings. This approach facilitates unobstructed optical access for Particle Image Velocimetry Measurements at any point and orientation. The specific gravity and kinematic viscosity of this liquid are 1.8 and $1.1 \times 10^{-6} m^2/s$, respectively.

Table 1 Geometric parameters and flow parameters

Casing diameter (D) (mm)	457.2
Hub radius (r_{hub}) (mm)	182.9
Rotor passage height from hub to endwall (L) (mm)	45.7
Rotor diameter (D_R) (mm)	453.6
Rotor blade chord (c) (mm)	102.6
Rotor blade span (H) (mm)	43.9
Rotor blade stagger angle (γ) (deg)	58.6
Rotor blade axial chord (c_A) (mm)	53.5
Measured tip clearance (h) (mm)	1.8 (0.0175c or 0.041H)
Axial casing groove diameter (mm)	34.8
Groove skew angle (deg)	45
Total number of grooves	60
Shaft speed (Ω) (rad s^{-1}) {RPM}	50.27 {480}
Rotor blade tip speed (U_T) (m s^{-1})	11.47
Flow coefficient ($\varphi=V_z/U_T$)	0.25, 0.38
Reynolds number ($U_T c / v$)	1.07×10^6

The original ACGs [13,17,18] as well as the dimensions and configurations of the present U and S grooves are illustrated in Figure 2. The axial position and circumferential distribution of the U and S grooves (Fig. 2c and 2d) are consistent with those of the original semi-circular ACGs (Fig. 2b). All have four grooves per rotor blade passage, and the same axial extent, 34.8mm (65% of the blade axial chord), of which 11.6 mm (33%) overlap with the blade leading edge, and the rest extending upstream of the blade. Both the grooves are open channel with ramped ends. They have 45° ramped inlets aligned in the positive circumferential direction up to the maximum depth of 9.09 mm (5.05 times the tip gap and 20% of the span). This ramp angle has been selected to be like that of the original ACGs. The outlets of both grooves at their upstream end are also ramped at 45°. The exit from the U grooves is aligned in the negative circumferential direction, and that of the S is directed in the positive circumferential direction. All the results are presented in a cylindrical coordinate system (r, θ, z), with the corresponding instantaneous velocity components denoted as u_r, u_θ, u_z, and the ensemble-averaged quantities as U_r, U_θ, U_z. The origin of the coordinate system is located at the center of the shaft ($r=0$), with $z=0$ coinciding with the blade leading edge.

The measurements have been performed at rotor speed of 480 RPM, corresponding to a Reynolds number based on the blade chord length and tip speed of 1.07×10^6. The flow rate is measured by integrating the velocity measured along the radius by translating a pitot tube in the return channel of the facility. The flow is driven primarily by the test compressor, which is connected to a 60 hp (44.74 kW) motor, with an additional
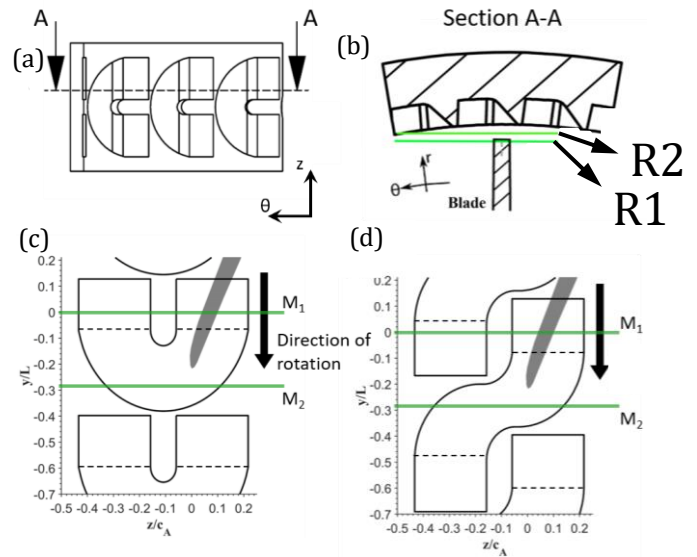

Figure 4: (a) The U grooves in a radial plane indicating the AA section, (b) Section AA showing the location of radial (θ, z) PIV planes, with R1 aligned with the blade tip, and R2 with the tip gap, (c, d) Radial views of the U and S groove indicating the location of meridional PIV planes M1 and M2.

auxiliary 20 hp (14.9 kW) pump used for extending the range of flow conditions. The flowrate is varied by altering the resistance of the loop, and is specified as a dimensionless flow coefficient, $\varphi = V_z/U_T$, where V_Z is the average axial velocity in the blade passage area and U_T is the tip speed. For velocity measurements, the mean pressure in the loop is maintained at a level that prevents cavitation.

The Stereo Particle Image Velocimetry (SPIV) measurements have been performed in two radial and two meridional planes. As illustrated in Fig. 4b, one of the radial planes (R1) coincides with the blade tip, corresponding to 96% of rotor passage height (H), and the (R2) coincides with the tip gap, namely 0.98H. The meridional planes illustrated in Figs. 4c and 4d intersects the groove at two different location, denoted as M1 and M2, which are separated by $\Delta\theta$=3°. The M1 meridional plane intersects with inlet groove ramp (at ~70% of the total depth), and the M2 plane intersects the U groove near its base, and the S groove in the curved section connecting the inlet to the outlet. The data presented in this paper corresponds to flow coefficients of $\varphi=0.25$, and 0.38.

At each plane, data has been recorded at fourteen different rotor blade orientations relative to the groove, covering an entire blade passage. The blade phases are denoted as s/c, which indicate the location along the chord where plane M1 intersects with the blade chord, with $s/c=0$ corresponding to the blade leading edge. The imaging system is synchronized to different blade orientation using an encoder mounted on the rotor shaft. The fourteen phases are unequally spaced, with the spacing being smaller on either side of the s/c=0 phase. The SPIV optical setup and two-step calibration procedures [23] have been described in previous papers [e.g. 17,18]. The flow field is
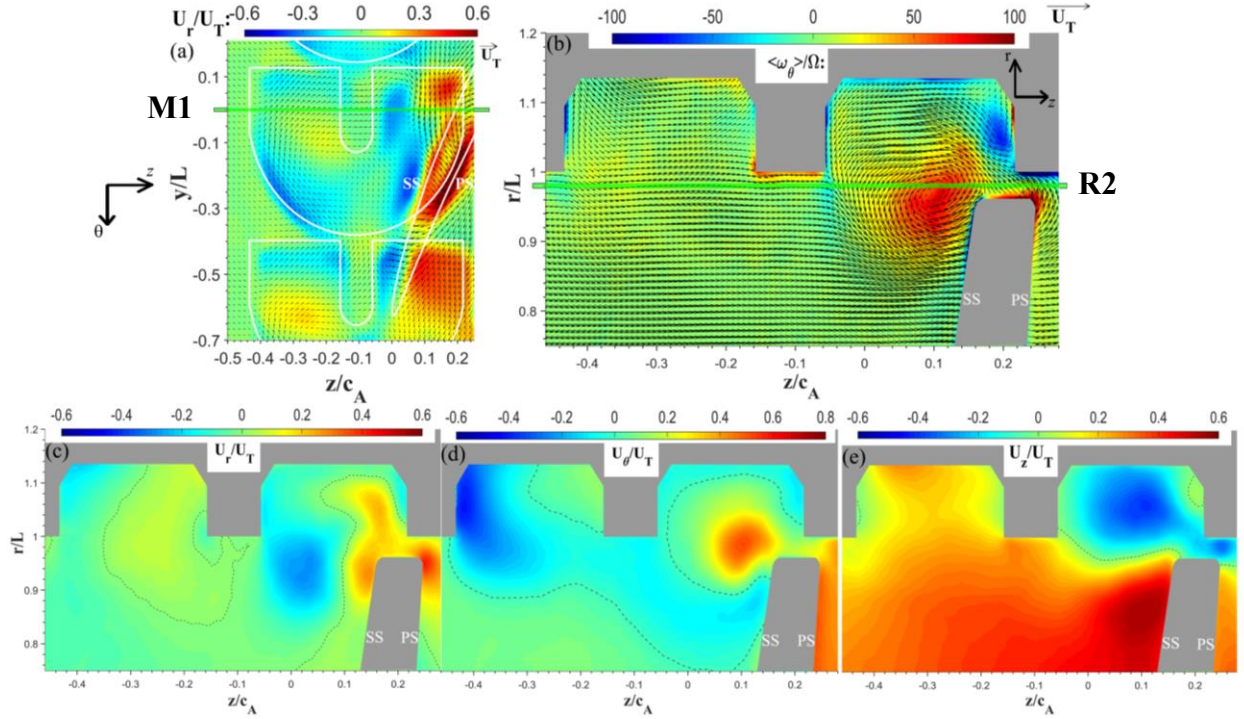
Figure 5: The ensemble averaged flow structure for the U groove at $\varphi=0.25$ and $s/c = 0.328$: (a) Distribution of U_r/U_T (color contours) and the in-plane velocity (U_θ, U_z) vectors in radial plane R2; (b-e) distributions of: (b) $<\omega_\theta>/\Omega$ contours and (U_r, U_z) vectors, (c) U_r/U_T, (d) U_θ/U_T, and (e) U_z/U_T in meridional plane M1. Corresponding reference vectors showing U_T are presented on the top right corners of (a, b).

illuminated by a 1 mm thick laser sheet expanded from a dual head 200mJ/pulse Nd:YAG laser beam. The flow is seeded with silver coated hollow glass sphere that have a mean diameter of 13μm and a specific gravity of 1.6, slightly lower than that of the liquid. The field of view of the radial planes are 40.12×41.2 mm, and the data have acquired using a pair of 2048×2048 pixels PCO.2000 cameras. The delay between exposures is 20μs, corresponding to a typical particle displacement of 8-12 pixels. After enhancement and filtering [31], multi-pass cross-correlation with a final interrogation window size of 24×24 pixels, and 50% overlap between windows, results in a vector spacing of 0.28mm. The meridional plane data have been recorded with a field of view of 44.57×45.13mm by a pair of Imperx B6640 CCD cameras, which have a pixel array of 6600×4400 pixels. For delay between exposures of 20μs, the typical particle displacement is 12-20 pixels. Hence, the final window size is 32×32 pixels with 50% overlap, resulting in a vector spacing of 0.14 mm. For the radial planes, 500 instantaneous realizations have been recorded for each plane, phase, and flow rate. In the meridional planes, the data for each planes and flow rate consist of 1000 realization for four rotor phases, and 200 for the other ten, the former for future analysis of turbulence in the passage. These numbers have been selected based on convergence tests. The discussions in this paper are based on the phase-averaged data over 200 realizations. Based on our previous studies [23], the uncertainty in instantaneous velocity is about 0.1 pixel, corresponding to 0.4–0.8% of the tip speed, provided there are more than five particles in each interrogation window.

RESULTS AND DISCUSSIONS
Prominent Features at $\varphi=0.25$

Figures 5-13 show and compare the flow structures around the U and S grooves at $\varphi=0.25$. Sample M1 cross sections showing distributions of all the velocity components and circumferential vorticity along with the corresponding radial velocity in the R2 planes are presented in Figures 5 and 6 for the U and S grooves respectively. The velocity components for the M2 planes are provided in Fig. 12. At this phase, the TLV is located partially within the groove entrance area (Fig. 5b and 6b). The area occupied by the vortex has a positive U_θ, but it is surrounded by low negative U_θ. The R2 planes (Fig. 5a and 6a) show that the radial velocity into the groove peaks along the pressure side of the blade, but is negative on the suction side owing to the influence of the TLV. In both cases, the axial velocity within the groove (Fig. 5e and 6e) is negative on the inlet side. The clear difference occurs on the exit (upstream) side, where U_θ is negative for the U groove, and positive for the S groove, as intended. Furthermore, magnitude of negative radial velocity (outflow) is higher for the S groove along the upstream end of the exit channel, which causes a higher axial momentum deficit there.

The velocity distributions in the R2 plane for different phases (Fig. 7) facilitate a comparison of groove-passage flow
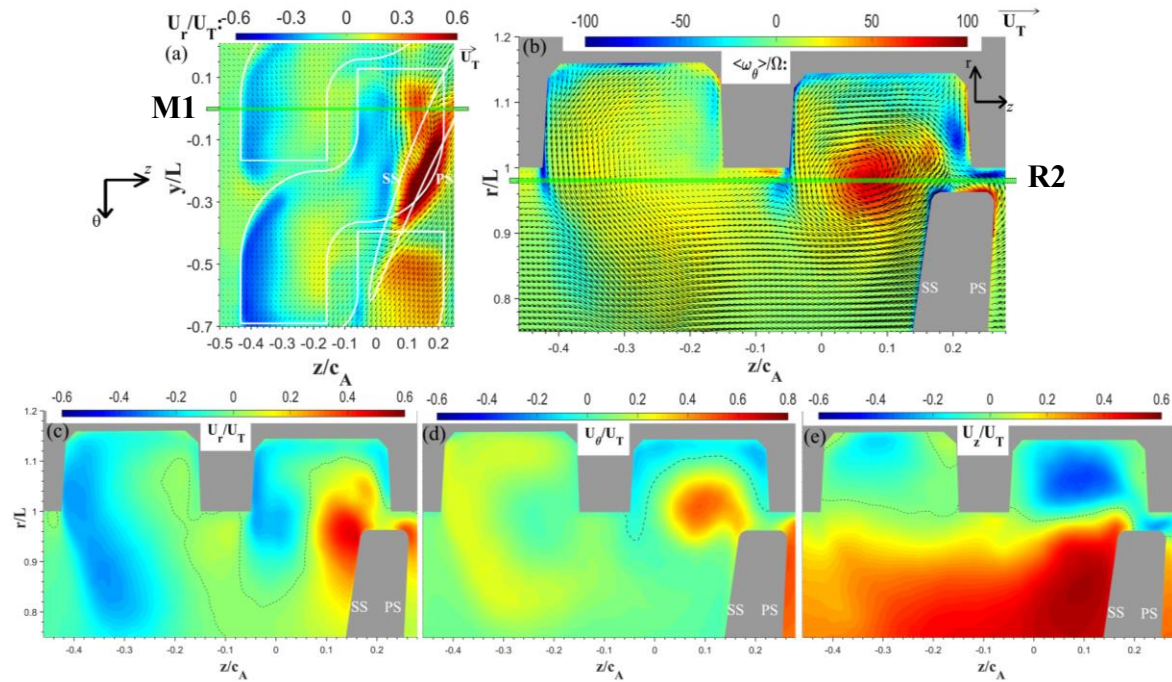
Figure 6: The ensemble averaged flow structure for the S groove at $\varphi=0.25$ and $s/c=0.328$. (a) Distribution of U_r/U_T (color contours) and (U_θ U_z) vectors in radial plane R2 ; and (b-e) distributions of: (b) $<\omega_\theta>/\Omega$ contours and (U_r, U_z) vectors, (c) U_r/U_T, (d) U_θ/U_T, and (e) U_z/U_T in meridional plane M1.

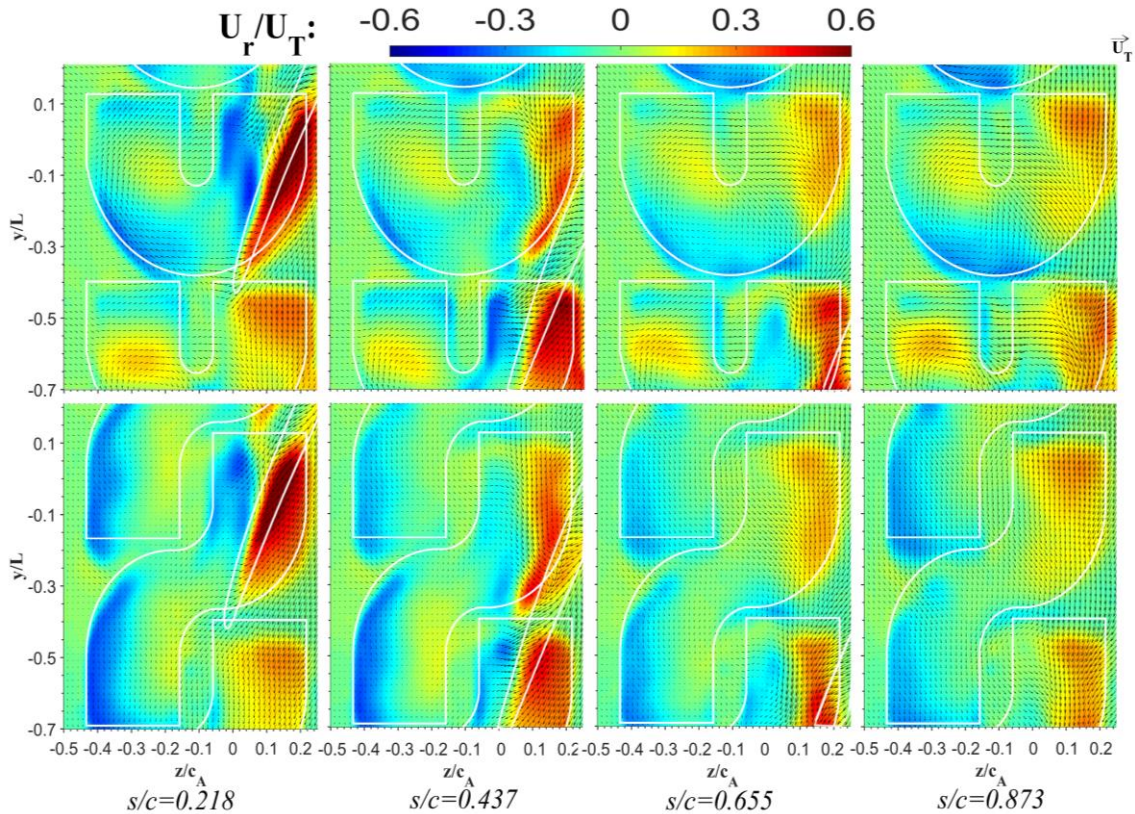Figure 7: Distributions of U_r/U_T (color contours) and in-plane velocity vectors in the R2 plane and at $\varphi=0.25$. (Top row) U groove, and (bottom row) S groove data. The phases are specified below each column. The corresponding locations of the blade tip (radially inward from the sample plane) and grooves are indicated with white solid lines. A reference U_T vector is shown on top.
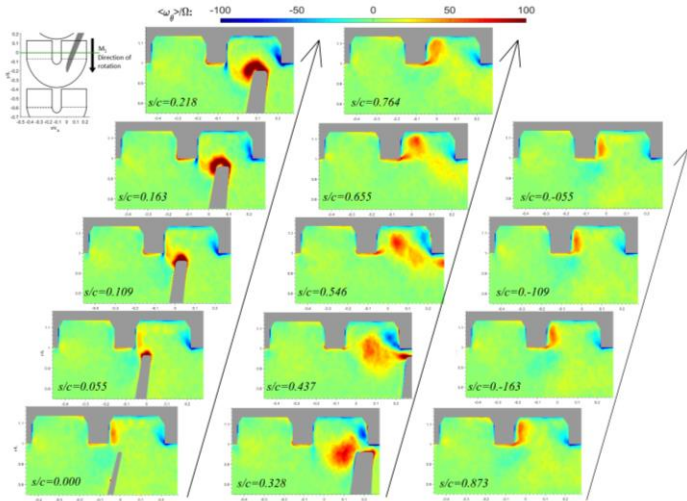
Figure 8: Evolution of circumferential vorticity with phase in the M1 plane for the U groove at $\varphi=0.25$.

Figure 9: Evolution of circumferential vorticity with phase in the M1 plane for the S groove at $\varphi=0.25$.

interaction trends for the U and S grooves. Prominent features include peak influx into the groove when its downstream end is exposed to the pressure side (PS) of the blade. However, inflow persists even when the blade is located far from the groove (e.g. $s/c=0.873$). While the outflow from the S groove occurs along the upstream end of the exit channel and persists for all phases, as intended, the outflow ($U_r<0$) from the U groove peaks near the base of the groove, and its location fluctuates with phase. It appears that the flow within the U groove does not seem to complete the turn towards the upstream end, and in fact, for broad parts of the upstream end, the radial velocity is directed into the groove. The different locations of peak outflow can be seen in the M1 planes for the S groove (Fig. 6c), and in the M2 planes for the U groove (Fig. 12).

Prominent features in the evolution of TLV entrainment into the groove are depicted in Figs. 8 and 9 for the U and S grooves, respectively. In both cases, the TLV appears to roll up above the blade tip, and is subsequently entrained into the groove. Flow separation of the backward leakage flow at the downstream end of the groove (evident also in Figures 5b and
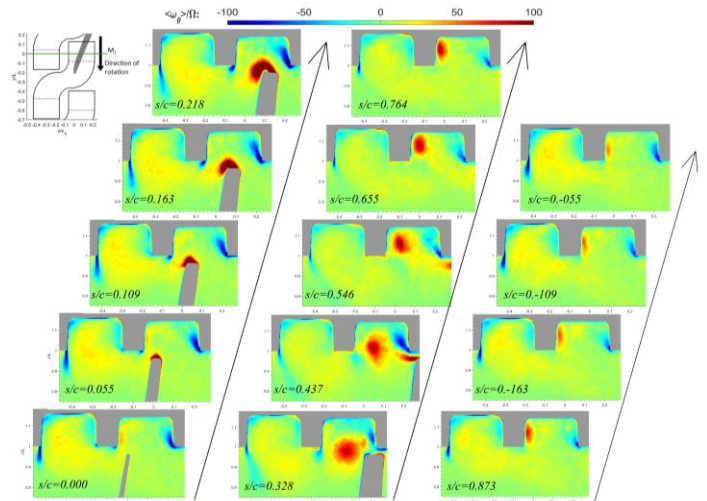
6b) generates a layer of negative vorticity, which is also entrained. In [17,18], the resulting negative vortex is referred to a "corner vortex". With increasing phase, the TLV appears to migrate to the upstream top corner of the inlet channel, and its strength diminishes owing to circumferential (out of plane) transport of parts of this vortex within the groove. The remaining part is located in a region with very low circumferential flow; hence it is transported very slowly. In both cases, the last remnants of the previous TLV are entrained into the passage by the next blade. As noted above, the primary differences occur along the exit (upstream) channel, where the peak radial outflow jetting from the S groove, which coincides with the M1 planes, generates a negative vorticity layer extending radially inward into the passage. The outflow brings with it a broad area with positive vorticity into the passage, which also evident in Fig. 6.

Other differences in groove effect are highlighted by comparing the circumferential velocity distributions, samples of which are provided in Fig. 10 and 11, respectively. A more detailed set showing the entire evolution of U_θ for the U groove is provided in the appendix (Fig. A1). In both cases, the flow entrained from the pressure side has high positive U_θ, consistent
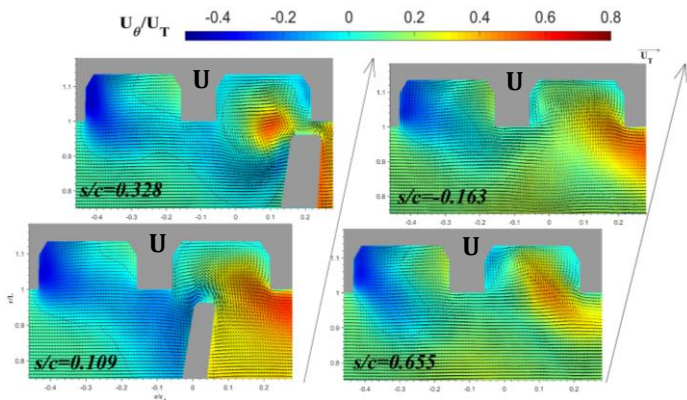

Figure 10: Evolution of the U_θ/U_T (color contours) and in-plane (U_r, U_z) velocity vectors with phase in the M1 plane of the U groove at $\varphi=0.25$.
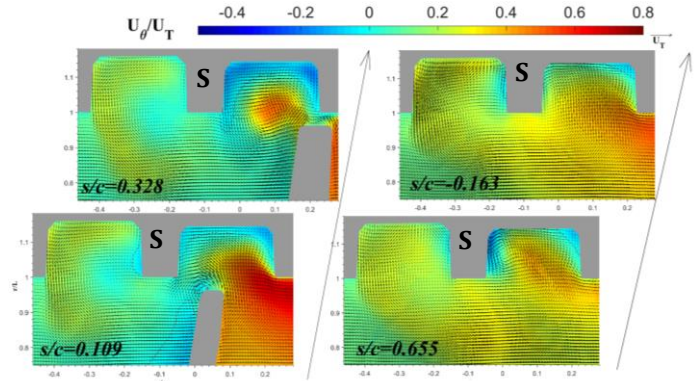

Figure 11: Evolution of the U_θ/U_T (color contours) and in-plane (U_r, U_z) velocity vectors with phase in the M1 plane of the S groove at $\varphi=0.25$.
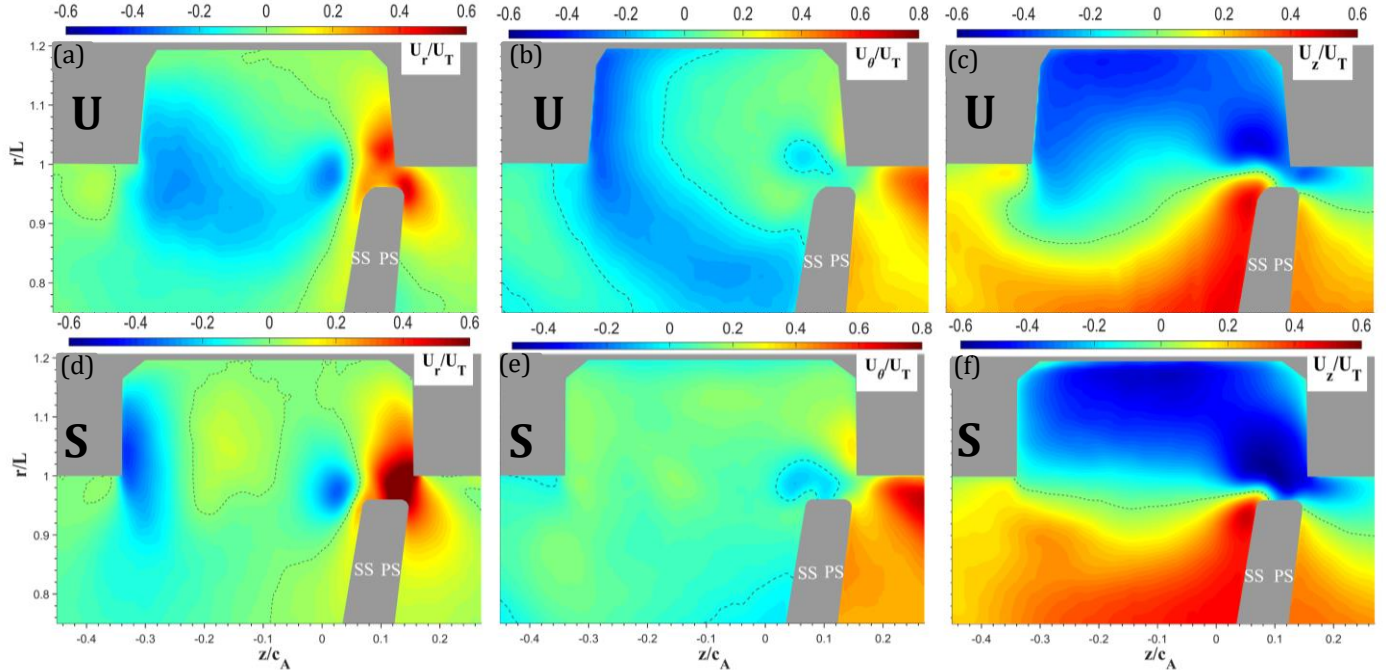
Figure 12: Sample comparison between the distributions of (a, d) U_r/U_T, (b, e) U_θ/U_T, and (c, f) U_z/U_T in the M2 plane: (top row, a-c) U groove, data, and (bottom row, d-f) S groove data. φ=0.25, and s/c=0.328.
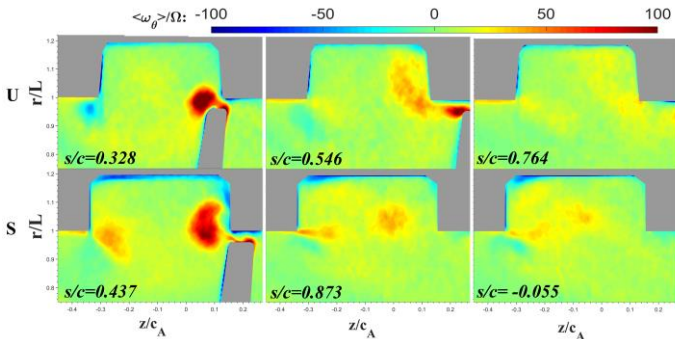

Figure 13: Selected distributions of $<\omega_\theta>/\Omega$ in the M2 plane at the indicated phases and at φ=0.25 for the: (top row) U groove, and (bottom row) S groove.

with the alignment of the inlet. In contrast, while the outflow jetting from the S groove has U_θ>0, the slower outflow from the U groove (at least in the M1 plane) has U_θ<0. This flow appears to be entrained straight into the SS of the blade at low s/c (e.g. s/c=0.109). Another notable feature include existence of axial gradients in U_θ in the inlet channel, implying that while the bulk of the entrained flow and TLV migrate circumferentially in the groove, the low and sometimes negative velocity at the upstream corner (of the inlet) causes the abovementioned remnants of the TLV to remain there until the next blade arrives.

Shifting to the M2 plane, i.e. close to area where the outflow from the U groove peaks and the outflow from the S groove is limited (see Fig. 7), Fig. 12 compares the three velocity components for the same sample phase. Here, the radial outflow extends over most of the U groove except for the immediate vicinity of the blade. The upstream half of this downflow already

has U_θ <0, indicating that the flow has already turned to the negative circumferential direction within the groove, as designed, although it exits earlier than expected. The impact of this U_θ <0 jet extends to beyond a quarter of the blade passage, and it creates a significant axial velocity deficit up to r/L=0.82 (Fig. 12c). It also influences the flow in the M1 plane, where the jet impinges on the blade SS (Fig. 10, s/c=0.109), as discussed before. In contrast, in this plane the outflow from the S groove is limited to its upstream end, and the associated circumferential velocity is positive, but low, almost everywhere, as the flow migrates from the inlet to the outlet channel. The local velocity deficit is significantly lower than that of the U groove. Finally, note that the axial and radial velocity gradients near the SS of the blade for both cases are caused by the TLV. Corresponding comparisons of sample vorticity distributions (Fig. 13) highlights differences in the TLV in the M2 plane. In the U groove, the vortex rolls up (s/c=0.328), entrained in part into the downstream end of the channel (s/c=0.546), but then disappears. In contrast, owing to low radial velocity in the middle of the S groove, the TLV remnants remain in the channel all the way to s/c=-0.055, i.e. when the next blade arrives. The implications of the findings summarized in this section on stall suppression are discussed in the discussion section.

Prominent Features at φ=0.38

Aimed at understanding the mechanisms affecting the differences in efficiency, this section examines the groove-passage flow interactions at high flow rate corresponding to BEP of the untreated endwall (Fig. 3). The results presented in Figs. 14-17 focus on specific flow features that might influence the machine performance. While the radial velocity distributions (Fig. 14) demonstrate that the interactions of the passage flow
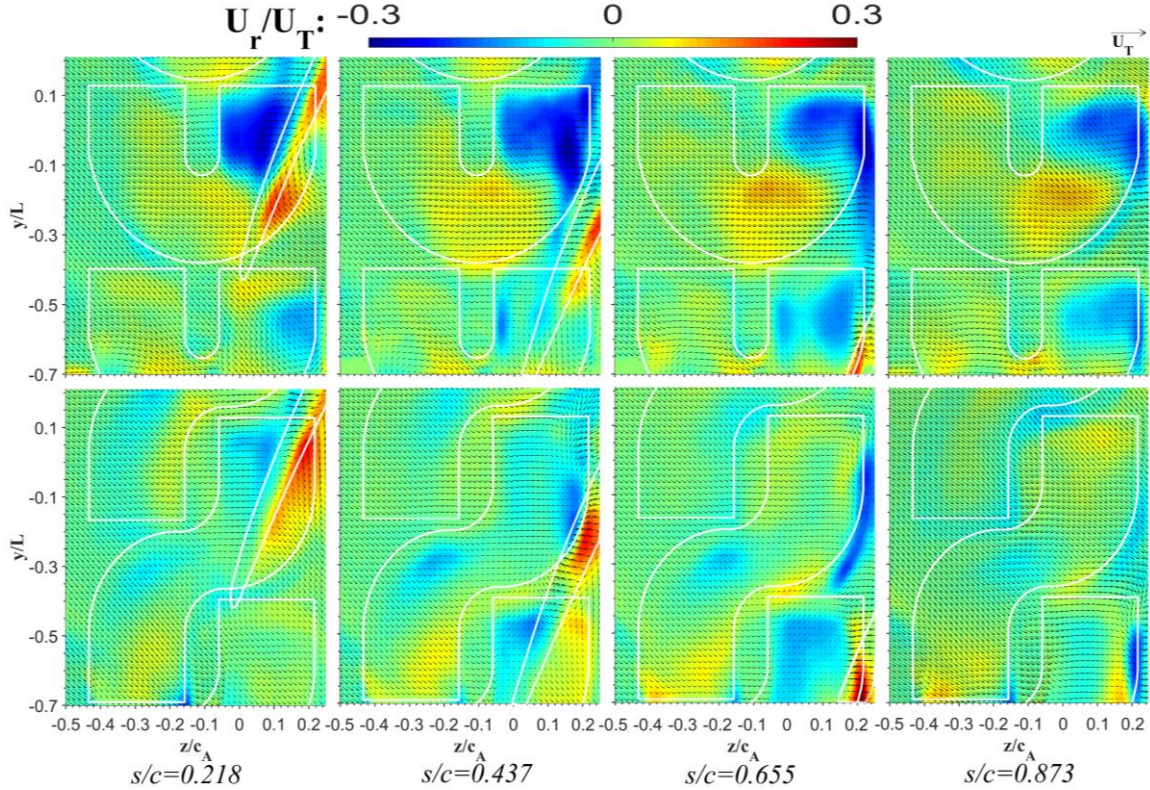
Figure 14: Distributions of U_r/U_T (color contours) and in-plane velocity vectors in the R2 plane and at $\varphi=0.38$: (Top row) U groove, and (bottom row) S groove data. The corresponding locations of the blade tip and the grooves are indicated with white solid lines.

with the grooves are weakened substantially for both grooves (compared to those of $\varphi=0.25$), they also show striking differences between the U and S grooves. For example, for all phases the inflow into the U groove ($U_r>0$) is centered around the base of the groove, and the outflow ($U_r<0$) seems to be concentrated in the downstream part of the channel, in exact contrast to the interactions observed at low flow rates. Only when the U groove is exposed to the blade PS ($s/c=0.218$ and 0.437), there is also inflow from the downstream corner of the groove, and even then, U_r is negative in parts of the PS. For the most part, the inflow and outflow from the upstream end of the U groove are weak. As for the S groove, the interactions with the passage flow seem to be concentrated around the blade tip, with inflow from the PS, which turns immediately back to the passage on the SS. This inflow seems to be stronger than that of the U groove. In other locations, the interactions of the S groove with the passage appear to be weak, with slow inflow at the upstream end and outflow in the middle of the passage. There is also a signature of secondary flow structures around the downstream end of this groove even when the blade is not located nearby, which is discussed later.

Comparisons between velocity and vorticity distribution in the M1 plane are presented in Fig. 15, representing conditions in which the blade tip is located near the grooves, and in Fig. 16 when the blade tip is located downstream. Fig. 15a shows that for the U groove, the radial velocity in the downstream channel is mostly negative even along the PS, causing an axial

momentum deficit there, and a shear layer that extends radially inward from the downstream wall into the passage. The TLV with its induced $U_r>0$ is confined to a small area near the PS tip (Fig. 15d). The circumferential velocity is negative, consistent with the flow entering the groove from its base, as Fig. 14 shows, and exiting from the downstream part of the groove. In the upstream part of the channel, there seems to be a circulating flow, with minimal impact on the axial momentum, and the shear layer at the interface with the passage appears to be similar to a cavity flow. As for the S groove, while $U_r>0$ in the part exposed to the blade PS, its magnitude is quite low except for very close to the blade tip, where the TLV begins to roll up. These trends suggest that the blade loading in this part of the blade is quite low. The rest of the interactions with the passage appear to be limited, showing nearly horizontal shear layers, and minimal impact on the axial velocity distribution. When the blade tip is not located near the groove, the downstream end of the U groove is filled with a radially inward, and circumferentially negative flow, i.e. it is aligned in the opposite direction to the main swirl in the passage. Furthermore, this outflow creates a radially-aligned shear layer extending from the downstream end of the groove, and an axial momentum deficit. Considering the radial gradients in U_θ, this flow also has negative axial vorticity, whose influence will be discussed later. In contrast, there is very limited interaction between the S groove and the passage flow at high flow rate, with the horizontal shear layers on both sides of the groove resembling cavity flows with internal circulation.
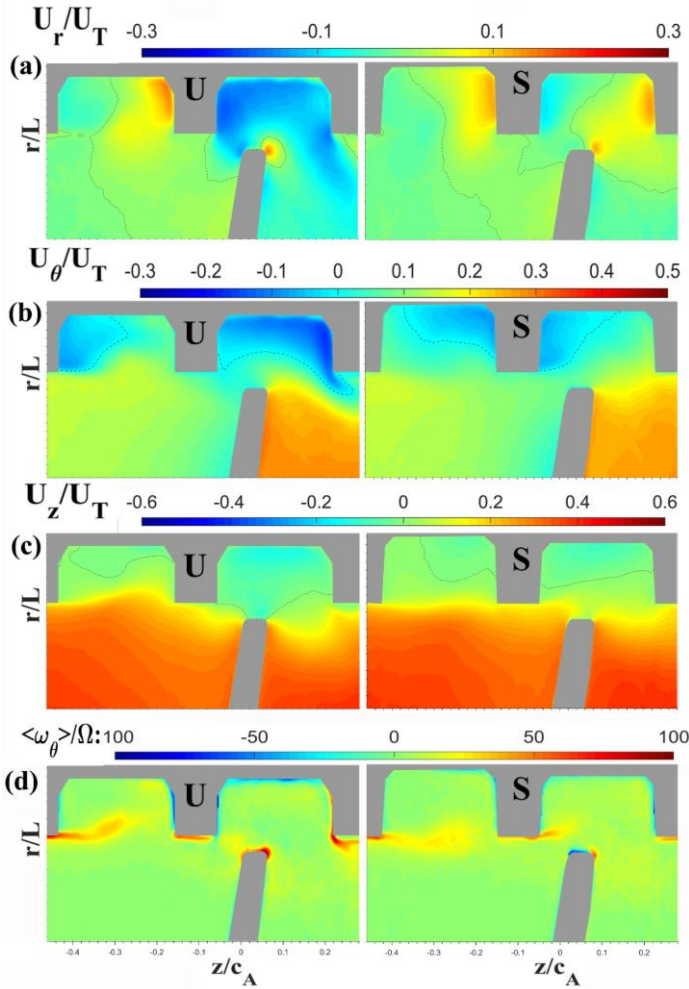
9

Figure 15: Distributions of: (a) U_r/U_T, (b) U_θ/U_T, and (c) U_z/U_T, and (d) $<\omega_\theta>/\Omega$ in plane M1 at $\varphi=0.38$, and $s/c=0.109$ for the: (left Column) U groove, and (right column) S groove. The dotted lines in (a-c) show the location of zero velocity component.

Figure 16: Distributions of: (a) U_r/U_T, (b) U_θ/U_T, and (c) U_z/U_T, and (d) $<\omega_\theta>/\Omega$ in plane M1 at $\varphi=0.38$, and $s/c=0.873$ for the: (left Column) U groove, and (right column) S groove. The dotted lines in (a-c) show the location of zero velocity component.

Finally, Fig. 17 compares selected vorticity distributions aimed at comparing the evolution of the TLV once it starts rolling up. Several trends are evident. First, in both cases, and for all phases, there is no evidence of significant entrainment of the TLV into the grooves. Second, the area occupied by the TLV is larger for the U groove. Third, the previously discussed corner vortex with negative vorticity develops as the leakage flow separates along the downstream end of the grooves. At $s/c=0.546$, the TLVs appear to entrain the corner vortex into the passage. In [17,32], it is demonstrated that interactions between the corner vortex generated in the semicircular grooves and the TLV cause TLV fragmentation and expansion as well as an increase in the turbulence level in the tip region.

Flow angles around the leading edge of the blade.

Fig. 18 compares sample distributions of inflow and outflow from the present grooves to that of the previously studied semicircular ACGs, all for $\varphi=0.25$ and the R1 (blade tip) plane. All show peak inflow when the blade PS is aligned with the
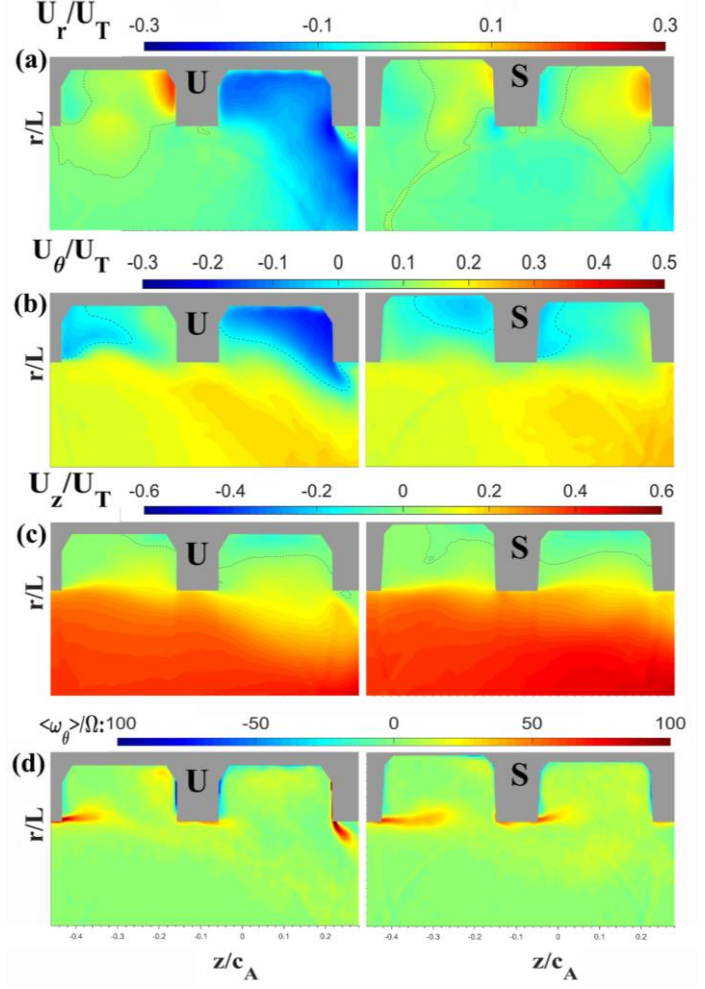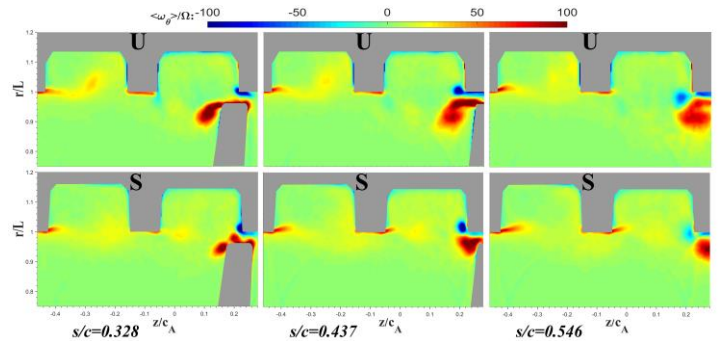

Figure 17: A comparison between selected distributions of $<\omega_\theta>/\Omega$ in the M1 plane at $\varphi=0.38$ for the: (top row) U groove, and (bottom row) S groove.

downstream end of the groove, signature of the TLV with positive and negative U_r along the SS, and outflow further upstream. For the S and semicircular grooves, this outflow is confined to the upstream end, while for the U groove, it is
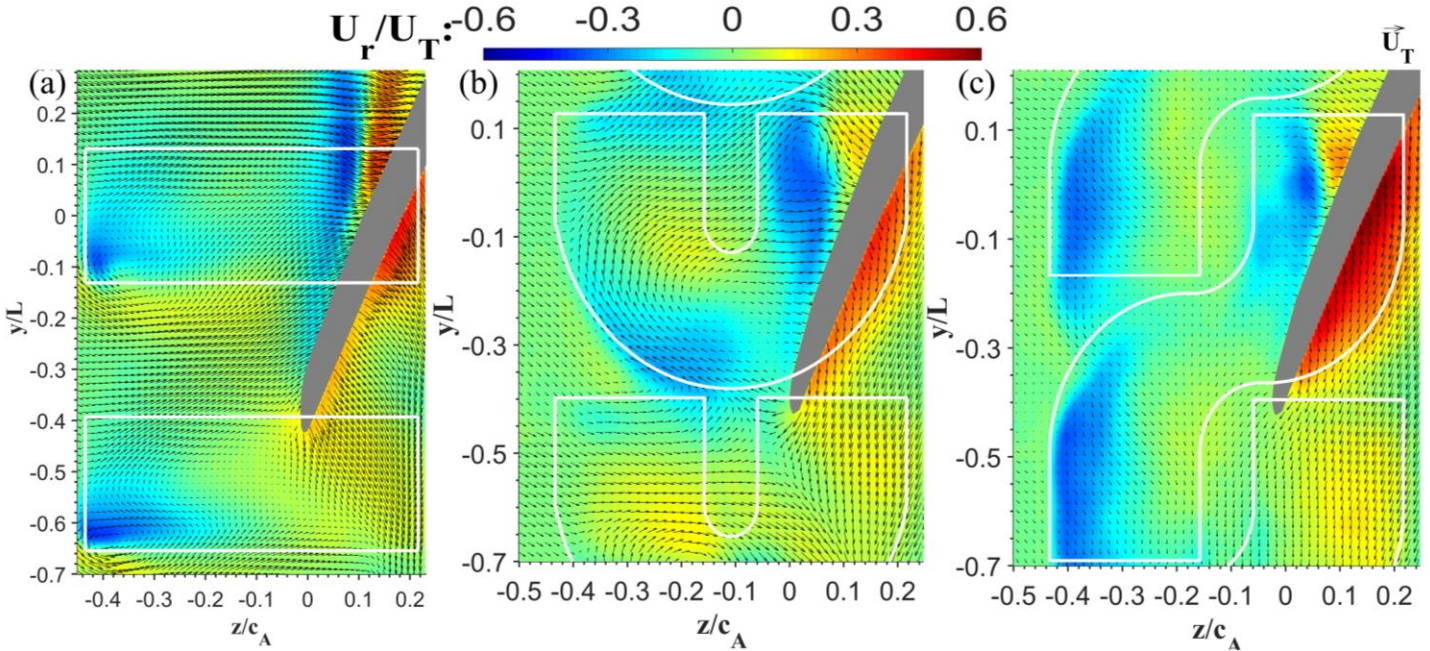
10   Copyright © 2020 by ASME

Figure 18: A sample comparison of U_r/U_T (color contours) and in-plane velocity vectors in the R1 plane (coinciding with blade tip) at $\varphi=0.25$ and $s/c = 0.218$: (a) semicircular ACGs, (b) U grooves, and (c) S grooves.
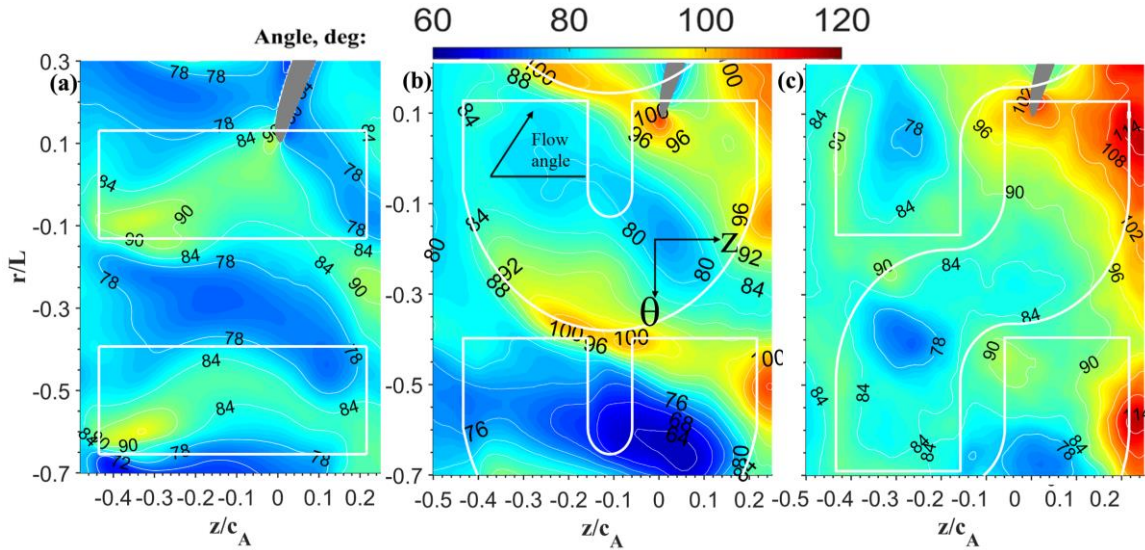

Figure 19: A Comparison of flow angles in the R1 plane at $\varphi=0.25$ and $s/c=-0.055$: (a) semicircular ACGs, (b) U grooves, and (c) S grooves.

distributed along the base of the groove. By design, the outflow from the U and semicircular groove are aligned in the negative circumferential direction, in contrast to the S groove. The resulting influence on the flow angle near the leading edge of the rotor blade is presented in Figures 19 and 20. This flow angle is calculated in the blade reference plane from the axial and circumferential velocity components. As is evident, in all cases, the flow angle fluctuates along the path of the blade leading edge, but owing to the direction of outflow from the grooves, the amplitude of these fluctuations is much higher for the U groove, varying between 64° to 100°. In contrast, for the S groove, excluding the immediate vicinity of the blade (which is

influenced by the local flow), the flow angle fluctuates only from about 76° to 90°. The amplitude of fluctuations for the semicircular grooves appears to fall between the other two extremes.

The radial extent of these fluctuations is shown in figure 20, where the results are also compared to those of the circumferentially non-varying angle for the untreated end wall. The region influenced by the periodic flow angle oscillations for the U groove extends to $r/L<0.8$, consistent with the extent of jetting outflow discussed before. Such oscillations, from an angle that is nearly 20 degrees smaller than that of the untreated endwall, to an angle that is 20 degrees higher than the smooth
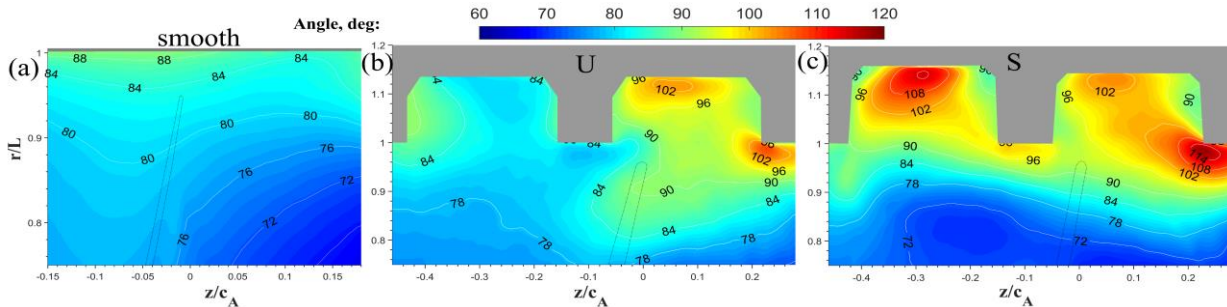
Figure 20: A comparison of of flow angles in the M1 plane at $\varphi=0.25$ and $s/c=-0.055$: (a) smooth endwall, (b) U grooves, and (c) S grooves. The dotted lines indicate the location of the blade leading edge about to reach the sample plane. Note the differences in field of view.

endwall values, is expected to cause periodic variations in blade loading, and presumably have a positive effect on the flow stability. The flow angle fluctuations for the S groove only varies by 10 degrees from the smooth wall values, and its radial extent is also smaller. These observations are consistent with the greater effect of the U groove on the flow stability.

The samples provided for high flow rate ($\varphi=0.38$) in Figure 21, also for the blade tip radial plane, show that the amplitude of flow angle fluctuations is much milder than those of low flow rate, as expected. However, the radial outflow with negative U_θ and low axial velocity still create a region with high flow angle along the downstream end of the U groove. In contrast, the region of inflow along the base of the U groove reduces the flow angle there. These interactions presumably generate undesirable variations in blade loading close to the BEP.

Impact on the flow downstream of the grooves

Figure 22 shows sample cavitation image visualizing the TLV and backflow vortices (BFVs)[19] downstream of the U groove at high flow rate. These images are obtained by reducing
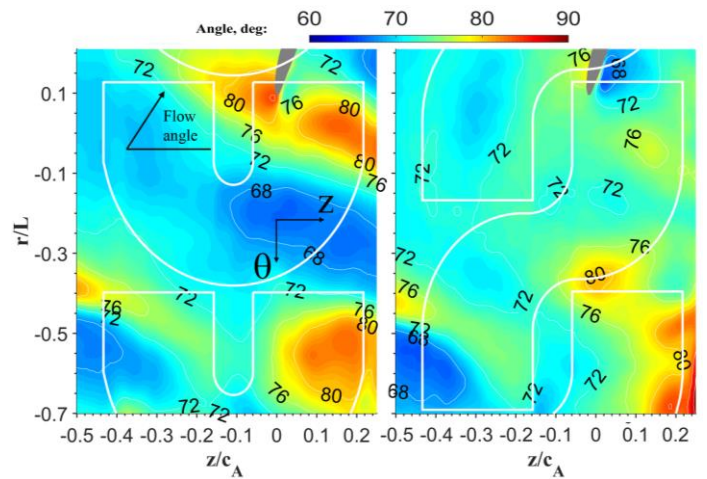

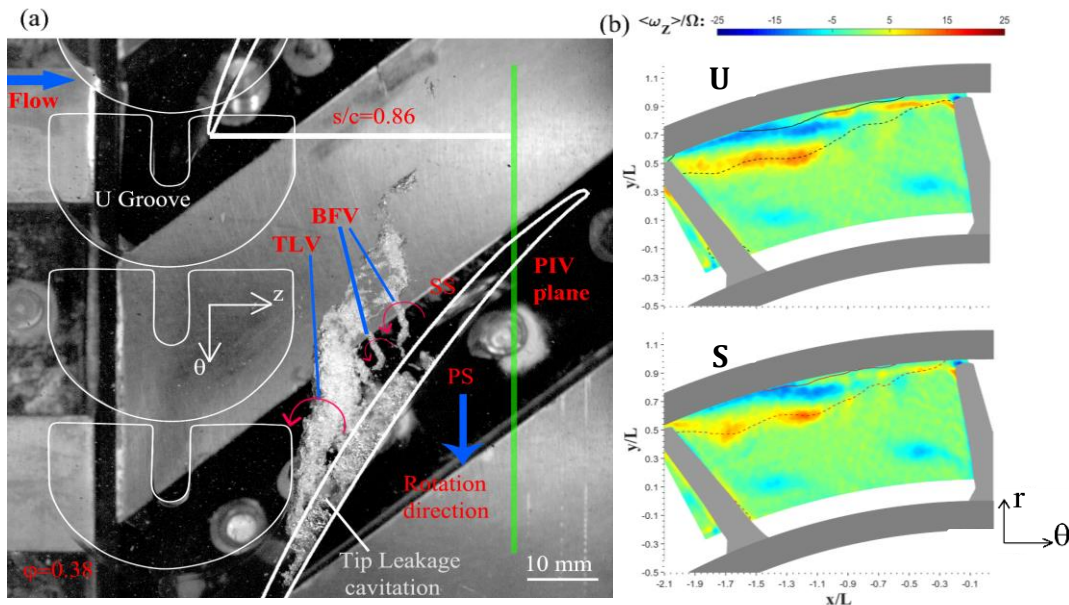Figure 21: A comparison of flow angles in the R1 plane at $\varphi=0.38$ and $s/c=-0.055$.

Figure 22: (a) A sample image of the cavitating vortices downstream of the U groove illustrating the orientation of the TLV and the BFV, and location of the PIV axial plane at 86% of the chord; and (b) distributions of $<\omega_z>/\Omega$ at $\varphi=0.38$ for the: (top) U groove, and (bottom) S groove [20].
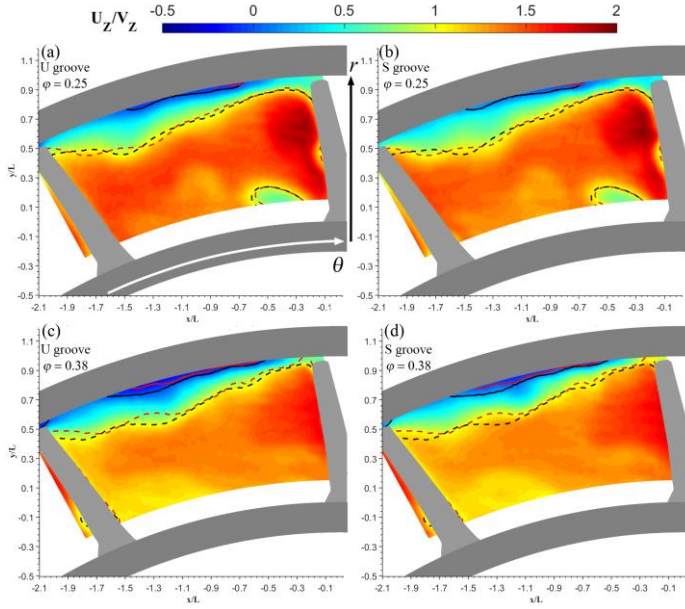
Figure 23: Distributions of U_z/V_Z at (top row) $\varphi=0.25$, and (bottom row) $\varphi=0.38$ for the: (left column) U groove, and (right column) S groove. Dashed lines: $U_z/V_Z=1$; solid lines: $U_z/V_Z=0$. Black lines correspond to the U groove and red lines to the S groove[20].

the pressure in the entire facility causing cavitation in the low-pressure cores of vortices. We have used this approach before [17,18,19,23,24] and have even shown that the TLV trajectory obtained by PIV (at higher pressures) matches that visualized by the cavitation [33]. The arrows illustrate the direction of rotation of the TLV and the BFVs. In the indicated axial plane located near the blade trailing edge, the TLV projection has a negative axial vorticity, and the BFVs have positive axial vorticity. The sample axial vorticity distributions presented in Fig. 22b show two layers of vorticity. The radially inner one, which is associated with the BFVs, has positive values, and the outer one, which is associated with the TLV signature, has negative values. The corresponding distributions of U_z and U_θ, which are presented in figure 23 and 24, show that for the same flow rate, the axial momentum deficits along the blade tip downstream of the U and S grooves, are not substantially different. In contrast, the circumferential velocity components differ significantly. They are higher for the U groove at high flow rate and for the S groove at low flow rates. It appears, as mentioned in the introduction, that reduced performance is associated with increased U_θ near the trailing edge. Considering that the elevated U_θ regions are bounded between the positive (BFV) and negative (TLV) axial vorticity layers, it appears that this phenomenon is caused by flow induced by these dominant flow structures. Since the BFVs roll up along the line of radial gradients in U_θ under the TLV [19] their strength is expected to be affected by suction into and injection from the grooves. Increased suction into the groove at low flow rates reduces the BFV strength, hence the circumferential velocity downstream of the grooves. Since the U groove is more effective at low flow rates, the magnitude of U_θ downstream is expected (presumably) to be lower. In contrast, at
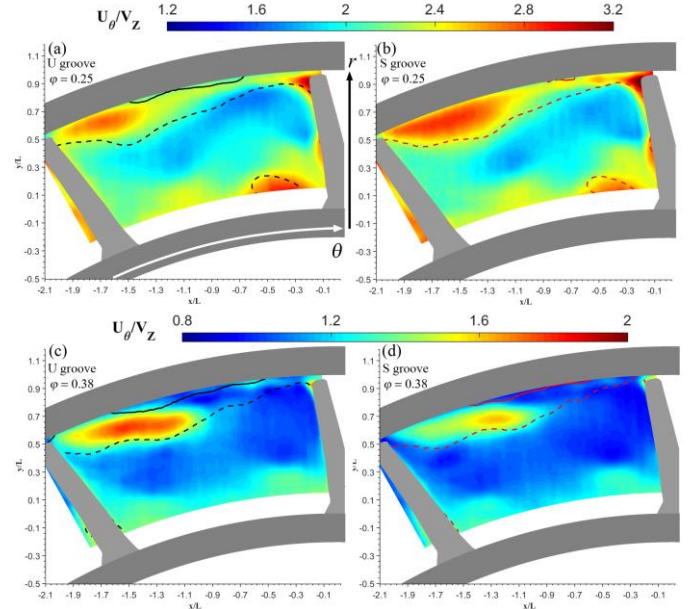

Figure 24: Distributions of U_θ/V_Z. For conditions and definitions, see Figure 23.

high flow rates, the previously discussed injection of flow with $U_\theta<0$ into the passage introduces a layer with negative axial vorticity along the endwall, which might contribute to the negative axial vorticity layer seen along the endwall in Fig. 22 (in addition to the TLV), and to the associated increase in U_θ. Hence, the velocity distributions near the trailing edge could be directly linked to the groove-passage flow interactions.

CONCLUSIONS

The detailed velocity measurements at different radial and meridional planes enables us to understand how the groove-passage flow interactions affect the machine stability at low flow rates, and its efficiency at high flow rates. By comparing the flow structures generated by the U and S grooves, and keeping in mind the results obtained for the previously examined semicircular ACG, this study focuses on the impact of the outflow from the groove on the machine performance. The performance tests indicate that an outflow aligned in the negative circumferential direction is more effective in delaying the onset of stall. The flow measurements suggest that this trend is associated with the substantially higher fluctuations in flow angle around the leading edge of the blade. For the present setup, the affected region extends to as much as the upper 25% of the rotor passage, as the flow with $U_\theta<0$ jets out of the groove and impinges on the blade suction side. Yet, even when the outflow is aligned in the positive circumferential direction, the S groves still achieve a considerable delay in the onset of stall, but not to the same extent as the U groove.

In terms of flow details, consistent with previous observations, at low flowrates the inflow into both grooves peaks periodically when the blade pressure side (PS) faces the entrance (downstream side) to the grooves. This inflow rolls up into a large vortex that remains and lingers within the groove long after

13   Copyright © 2020 by ASME

the blade tip clear the groove. While the flow progression in the S groove follow expected trends, the outflow from the U groove does not occur in the expected region, with most of its flow jetting out near the base of the groove. In this regard, the primary outflow location should be similar to that of the J groove (Fig 3). Indeed, both grooves show similar performance at $\varphi=0.25$, the condition of the present velocity measurements. However, the performance of the U and J grooves become significantly different as the flow rate is reduced further (e.g. $\varphi<0.2$), suggesting that the location of outflow from the U groove changes, presumably to a region located closer the originally planned exit, with decreasing flow rate. This postulate motivates future measurements of the flow with the U and S grooves at $\varphi\sim0.2$, where the performance of these grooves differs significantly.

While the outflow from the S groove occurs at the expected exit channel, it jets out only from a narrow part of this channel aligned along in the upstream part of the groove. Hence, narrower grooves might achieve a similar effect on the flow stability. Furthermore, the inflow into and outflow from the S groove seem to have less circumferential variations than the other systems investigated to-date. The shape of this groove, and the flow induced by the S groove appears to be a "hybrid" of a circumferential and axial grooves, motivating further investigation of hybrid grooves.

Near BEP, the very limited interactions of the S groove with the flow passage is advantageous, since it maintains the performance and efficiency of the original untreated endwall. In contrast, the U groove continue to interact extensively with the passage flow in an unexpected fashion. The locations of both inflow and outflow reverse, with the inflow shifting to the base of the groove, and the outflow, still with $U_\theta<0$, occurring in the downstream end of this groove. The resulting jet has several adverse effects, including: (i) it expands the size of the area occupied by the TLV, similar to phenomena observed for the semicircular ACG (although for somewhat different reasons [17]), (ii) it causes an axial momentum deficit along the pressure side of the blade, (iii) it separates the flow along the downstream corner of the groove, and (iv) it increases the flow angle fluctuations near the blade leading edge. The impact of these phenomena persists all the way to the blade trailing edge. Hence, it is not surprising the U groove causes an efficiency loss at high flow rates. While possible methods for alleviating these effects are speculative at this point, they might involve prevention of flow into the groove near the base of the U groove. Future efforts will address these questions.

ACKNOWLEDGMENTS

NOMENCLATURE

|		
c	=	rotor blade tip chord
h	=	width of the rotor blade tip gap
H	=	rotor blade span
L	=	nominal distance from the hub to the inner casing endwall
p_{exit}	=	static pressure at stator outlet
p_{in}	=	static pressure at IGV inlet
Q	=	volumetric flow rate
r, θ, z	=	radial, circumferential, and axial coordinates
r^*	=	Normalized radial coordinate
s	=	rotor blade chordwise coordinate
T	=	motor input torque
u_r, u_θ, u_z	=	Instantaneous radial, circumferential and axial velocity
U_R, U_θ, U_Z	=	Ensemble averaged radial, circumferential and axial velocity
U_T	=	rotor blade tip speed
u'	=	velocity fluctuation
V_z	=	average axial velocity in the rotor passage
ρ	=	NaI solution density
φ	=	flow coefficient
η	=	efficiency
θ_{blade}	=	Circumferential angle of a rotor passage
ψ_{SS}	=	static-to-static pressure rise coefficient
ω_θ	=	circumferential vorticity
Ω	=	rotor angular velocity
$<\;>$		ensemble-averaged quantity
BFV	=	Back Flow Vortices
TLV	=	Tip leakage vortex
ACG	=	Axial Casing Grooves
IGV	=	Inlet guide vanes

APPENDIX
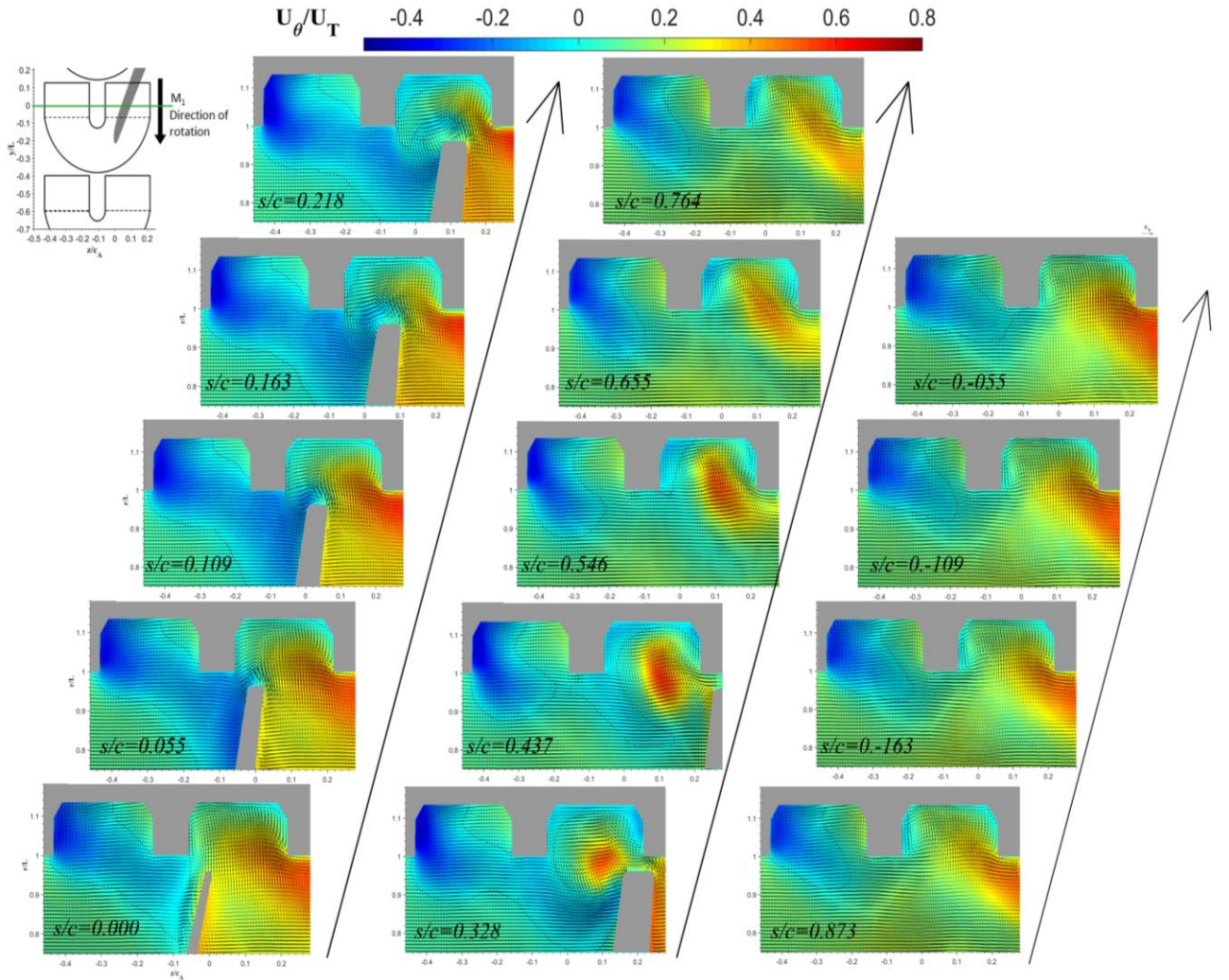
Figure A1: Evolution of U_θ/U_T (color contours) and in-plane velocity vectors (U_r, U_z) with phase in the M1 plane of U groove at $\varphi=0.25$.

REFERENCES

[1] Day, I. J., 1993, "Stall Inception in Axial Flow Compressors," J. Turbomach., **115**(1), pp. 1–9.

[2] Hathaway, M. D., 2007, "Passive Endwall Treatments for Enhancing Stability," NASA Techincal Rep., **NASA/TM-20**.

[3] Day, I. J., 2016, "Stall, Surge and 75 Years of Research," J. Turbomach., **138**(1), p. 011001.

[4] Prince, D. C., Wisler, D. C., and Hilvers, D. E., 1975, "A Study of Casing Treatment Stall Margin Improvement Phenomena," Volume 1A: General, ASME, p. V01AT01A059.

[5] Shabbir, A., and Adamczyk, J. J., 2005, "Flow Mechanism for Stall Margin Improvement due to Circumferential Casing Grooves on Axial Compressors," J. Turbomach., **127**(4), pp. 708–717.

[6] Weichert, S., Day, I., and Freeman, C., 2011, "Self-Regulating Casing Treatment for Axial Compressor Stability Enhancement," Asme Turbo Expo, ASME, Vancouver, Canada, p. 13.

[7] Prince D. C., J., Wisler, D. C., and Hilvers, D. E., 1975, "A Study of Casing Treatment Stall Margin improvement Phenomena," Trans ASME, pp. 75-GT-60.

[8] Fujita, H., and Takata, H., 1984, "A Study on Configurations of Casing Treatment for Axial Flow Compressors," Bull. JSME, **27**(230), pp. 1675–1681.

[9] Wilke, I., and Kau, H.-P., 2004, "A Numerical Investigation of the Flow Mechanisms in a High Pressure Compressor Front Stage With Axial Slots," J. Turbomach., **126**(3), pp. 339–349.

[10] Smith, G. D. J., and Cumpsty, N. A., 1984, "Flow Phenomena in Compressor Casing Treatment," J. Eng.

Gas Turbines Power, **106**(3), pp. 532–541.

[11] Brandstetter, C., Kegalj, M., Wartzek, F., Heinichen, F., and Schiffer, H.-P., 2014, "Stereo PIV Measurement of Flow Structures underneath an Axial-Slot Casing Treatment on a One and a Half Stage Transonic Compressor," 17th International Symposium on Applications of Laser Techniques to Fluid Mechanics, Lisbon, Portugal, pp. 1–18.

[12] Crook, A. J., Greitzer, E. M., Tan, C. S., and Adamczyk, J. J., 1993, "Numerical Simulation of Compressor Endwall and Casing Treatment Flow Phenomena," J. Turbomach., **115**(3), pp. 501–512.

[13] Müller, M. W., Schiffer, H.-P., Voges, M., and Hah, C., 2011, "Investigation of Passage Flow Features in a Transonic Compressor Rotor with Casing Treatments," Proceedings of ASME Turbo Expo 2011: Power for Land, Sea and Air, Vancouver, Canada, pp. 1–11.

[14] Osborn, W. M., Lewis, G. W. J., and Heidelberg, L. J., 1971, "Effect of Several Porous Casing Treatments on Stall Limit and on Overall Performance of an Axial-Flow Compressor Rotor," NASA Techincal Note, p. TN D-6537.

[15] Seitz, P. A., 1999, "Casing Treatment for Axial Flow Compressors," University of Cambridge.

[16] Beheshti, B. H., Teixeira, J. A., Ivey, P. C., Ghorbanian, K., and Farhanieh, B., 2004, "Parametric Study of Tip Clearance—Casing Treatment on Performance and Stability of a Transonic Axial Compressor," J. Turbomach., **126**(4), pp. 527–535.

[17] Chen, H., Li, Y., and Katz, J., 2018, "On the Interactions of a Rotor Blade Tip Flow With Axial Casing Grooves in an Axial Compressor Near the Best Efficiency Point," J. Turbomach., **141**(1), p. 011008.

[18] Chen, H., Li, Y., Koley, S. S., Doeller, N., and Katz, J., 2017, "An Experimental Study of Stall Suppression and Associated Changes to the Flow Structures in the Tip Region of an Axial Low Speed Fan Rotor by Axial Casing Grooves," J. Turbomach., **139**(12), p. 121010.

[19] Chen, H., Li, Y., Tan, D., and Katz, J., 2017, "Visualizations of Flow Structures in the Rotor Passage of an Axial Compressor at the Onset of Stall," J. Turbomach., **139**(4), p. 041008.

[20] Chen, H., Koley, S. S., Li, Y., and Katz, J., 2019, "Systematic Experimental evaluations aimed at optimizing the geometry of axial casing groove in a compressor," ASME Turbo Expo 2019: Turbomachinery Technical Conference and Exposition, pp GT2019-91050.

[21] Houghton, T., and Day, I., 2011, "Enhancing the Stability of Subsonic Compressors Using Casing Grooves," J. Turbomach., **133**(2), p. 021007.

[22] Wu, H., Tan, D., Miorini, R. L., and Katz, J., 2011, "Three-Dimensional Flow Structures and Associated Turbulence in the Tip Region of a Waterjet Pump Rotor Blade," Exp. Fluids, **51**(6), pp. 1721–1737.

[23] Miorini, R. L., Wu, H., and Katz, J., 2012, "The Internal Structure of the Tip Leakage Vortex Within the Rotor of an Axial Waterjet Pump," J. Turbomach., **134**(3), p. 031018.

[24] Tan, D., Li, Y., Wilkes, I., Miorini, R., and Katz, J., 2015, "Visualization and Time Resolved PIV Measurements of the Flow in the Tip Region of a Subsonic Compressor Rotor," J. Turbomach., **137**(4), p. 041007.

[25] Wu, H., Miorini, R. L., and Katz, J., 2011, "Measurements of the Tip Leakage Vortex Structures and Turbulence in the Meridional Plane of an Axial Water-Jet Pump," Exp. Fluids, **50**(4), pp. 989–1003.

[26] Wu, H., Miorini, R. L., Tan, D., and Katz, J., 2012, "Turbulence Within the Tip-Leakage Vortex of an Axial Waterjet Pump," AIAA J., **50**(11), pp. 2574–2587.

[27] Tan, D., Li, Y., Chen, H., Wilkes, I., and Katz, J., 2015, "The Three Dimensional Flow Structure and Turbulence in the Tip Region of an Axial Flow Compressor," ASME Turbo Expo 2015: Turbine Technical Conference and Exposition, pp. GT2015-43385.

[28] Li, Y., Chen, H., Tan, D., and Katz, J., 2016, "Effects of Tip Clearance and Operating Conditions on the Flow Structure and Reynolds Stresses within an Axial Compressor Rotor Passage," ASME Turbo Expo, pp. GT2016-57050.

[29] Hah, C., 2017, "Effects of Double-Leakage Tip Clearance Flow on the Performance of a Compressor Stage With a Large Rotor Tip Gap," J. Turbomach., **139**(6), p. 061006.

[30] Wieneke, B., 2005, "Stereo-PIV Using Self-Calibration on Particle Images," Exp. Fluids, **39**(2), pp. 267–280.

[31] Roth, G. I., and Katz, J., 2001, "Five Techniques for Increasing the Speed and Accuracy of PIV Interrogation," Meas. Sci. Technol., 12(3), pp. 238–245.

[32] Chen, H., Li, Y., Koley, S. S, and Katz, J., 2019,"Effects of axial casing grooves on the structure of turbulence in the tip region of an axial turbomachine rotor " ASME Turbo Expo 2020: Turbomachinery Technical Conference and Exposition, pp GT2020-15229.

[33] Li, Y., Chen, H., Tan, D. and Katz, J., 2019. On the Effects of Tip Clearance and Operating Condition on the Flow Structures Within an Axial Turbomachine Rotor Passage. *Journal of Turbomachinery*, *141*(11).